CAMBRIDGE
UNIVERSITY PRESS

RESEARCH ARTICLE

Workspace optimization of a humanoid robotic arm based on the multi-parameter plane model

Peng Sun[1] , YanBiao Li[1,*] , Kun Shuai[1], Yi Yue[2] and BaoChen Wei[3]

[1]College of Mechanical Engineering, Zhejiang University of Technology, Hangzhou 310023, China, [2]School of Mechanical and Automotive Engineering, Shanghai University of Engineering Science, Shanghai 201620, China, and [3]School of Mechanical Engineering, Shanghai Jiao Tong University, Shanghai 200240, China
*Corresponding author. E-mail: lybrory@zjut.edu.cn

Abstract

The paper deals with the workspace-based optimization of a novel humanoid robotic arm. The eight-degree-of-freedom hybrid manipulator that conforms to the kinematics characteristics of the human arm is briefly introduced. According to the structural features of this mechanism and the requirements of tasks in the complex environment, the workspace is divided into three parts, the orientation space of the humanoid shoulder joint, the position space of the humanoid elbow joint, and the active orientation space of the end-moving platform. Moreover, a multi-parameter planar model is proposed for the optimization problem with multidimensional parameters and highly nonlinear constraints. Based on the visualized optimization result, the coupling effect of each parameter on the corresponding workspace is clearly presented. Considering the compactness and the processing and assembling technology of this mechanism, a set of structural parameters satisfying the workspace-based optimization objective is obtained. Simulation results show that the corresponding workspace of the three parts has increased significantly by the factor of 1.45, 1.68, and 1.3, respectively.

1. Introduction

With the changes of service objects and developments of task demands, the applications for the advanced control algorithm and driving technologies of robotic arms are also increasing. However, the high sensitivity and maneuverability of the typical robotic arm is limited by an inherent characteristic that the joint actuators are mounted onto the arms themselves [1, 2]. Hence, in order to avoid this problem, scholars have conducted extensive research on the applications of parallel mechanisms and hybrid mechanisms in the field of robotic arms. Among them, the configuration synthesis [3, 4] and performance optimization [5, 6] of the mechanisms are one of the most important research contents.

Generally speaking, there are three types of mechanisms: serial mechanisms, parallel mechanisms, and hybrid mechanisms. The serial mechanism is the typical configuration of robotic arms with a large workspace and flexible movement [7]. However, the joint actuators are mounted onto the bottom of the link will cause a bulky mechanical structure, large moment of inertia, and low payload to weight ratio [8]. Compared with the serial mechanism, the parallel mechanism has a compact structure, and its multiple closed kinematic chains can provide greater stiffness, higher payload to weight ratio, reduced inertia, and higher precision [9, 10]. Although the parallel mechanism effectively compensates for the shortcomings of the serial mechanism, it also has the disadvantage of small workspace and large lateral size. The hybrid mechanism, which combines series mechanisms and parallel mechanisms through different structural configurations, exhibits broad application prospects. As such, the serial mechanism can provide a larger position space for the end manipulator, and the parallel mechanism can guarantee the stronger stiffness and greater load capacity of the entire mechanism as well as the higher positioning

(a)

(b)
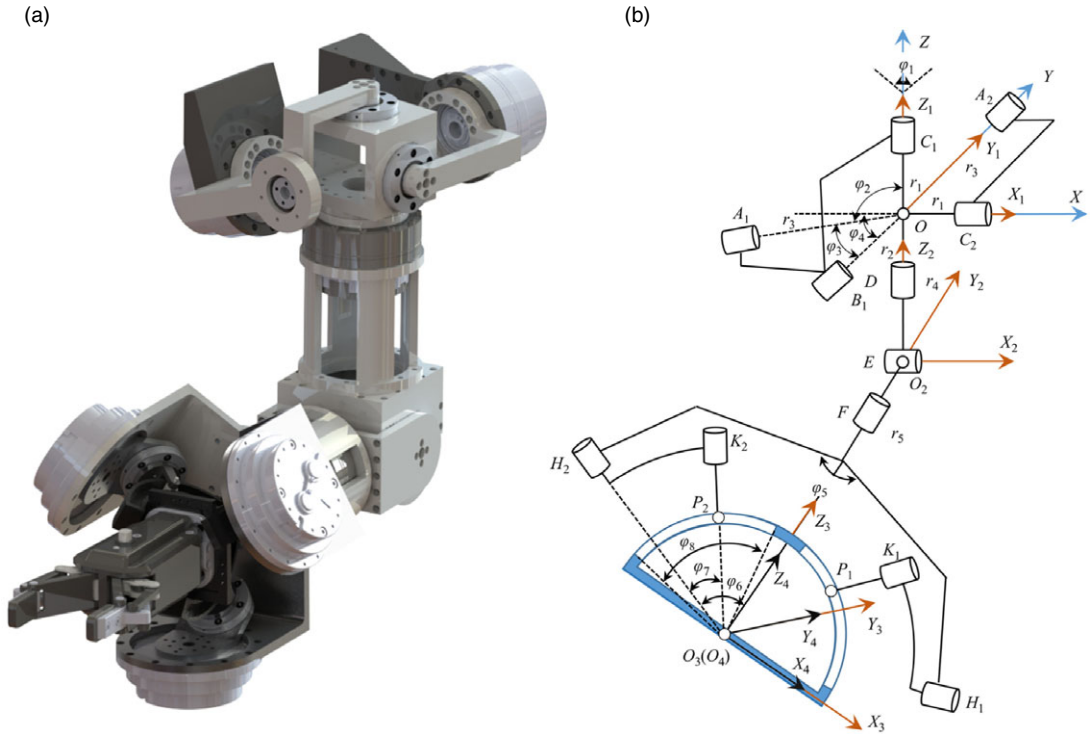
Figure 1. *Structural configuration of HRA (left arm): (a) Three-dimensional model; (b) mechanism diagram. The revolute pairs H_3 and K_3 and the prismatic pair P_3 are abnegated.*

precision. In our previous work [11, 12], a novel eight-degree-of-freedom hybrid humanoid robotic arm (HRA) is proposed to realize the kinematics characteristic of the human arm that is to cooperate with the hand to perform partial fine operations, as shown in Fig. 1(a).

After determining the configuration synthesis [3, 4] of mechanisms, the workspace analysis can be regarded as the first crucial step in the procedure of dimension synthesis [13, 14]. However, because the workspace is embedded in a six-dimensional space which cannot be represented graphically in a readable way, its rendering and evaluation are especially challenging. So far, there is no universal method to analyze and determine the boundary of the six-dimensional workspace, so dividing it into position space and orientation space is a feasible and recognized method. The position space refers to a space that the end-moving platform can reach with a certain or uncertain orientation, which can be depicted easily and directly. But the study of orientation space is very complicated, and its boundary is related to the position of the end-moving platform. Due to the coupling effect of position and orientation, how to express the execution ability of the workspace of the end-platform is a very meaningful matter. Guo et al. [15] used a transformation method to analyze a novel n (3RRlS) metamorphic serial-parallel manipulator with multiple working conditions. Vieira et al. [16] employed Monte Carlo algorithm to compute failure probabilities for a dense grid of manipulator workspace configurations of parallel manipulators under geometrical uncertainties. Masouleh et al. [17] proposed a new extension of growing neural gas network for obtaining the singularity-free workspace of planar parallel mechanisms. This subject has been extensively explored, and it is still under investigation in concrete applications.

On the other hand, in order to select a set of structural parameters for the ideal workspace and perfect performance, a multitude of effort has been made in the design optimization. The method of design optimization is roughly divided into two categories: one is to construct the dimension space [18, 19] of structural parameters and the other is to apply intelligent algorithms. The dimension space is a simple and direct design method that considers all indicators and can ensure the independence of each indicator,

but it is not suitable for handling the multi-parameter design. At present, many research studies have been carried out on this topic, and the commonly used optimal intelligent algorithms mainly include genetic algorithms [20, 21], differential evolution algorithms [22, 23], particle swarm algorithms [24, 25], ant colony algorithms [26]. The optimization complexity is increased due to the high nonlinearity of the optimization objective functions and structural parameters as well as the non-identity between the objective functions. The initial value selection of the intelligent algorithms has a great influence on the optimization result, and it cannot directly show the mapping relationship between performance indicators and structural parameters. Hence, designing a three-dimensional visualized dimension space and combining it with intelligent algorithms is a meaningful research.

In this work, we focus on the workspace-based optimization of the HRA. In Section 2, the structural parameters of each joint are defined, and the conclusions of the inverse displacement analysis are briefly listed. The humanoid shoulder joint (HSJ) and humanoid elbow joint (HEJ) determine the position space of the end-reference point and also provide a parasitic orientation for the end-moving platform. The revolute joint F of the HEJ and humanoid wrist joint (HWJ) determine the active orientation space of the end-moving platform. In Section 3, according to the structural characteristics of each joint, the constraint conditions of the workspace are set, and the workspace of each joint based on the initial structural parameters are illustrated. The HSJ allows the amplitude mobilization of the large arm, and the HEJ allows the upper limb to bend or stretch backward and the forearm to rotate along its longitudinal axis, and the HWJ and the end revolute joint of the HEJ realize flexible rotation of the hand in partial operations. In Section 4, a multi-parameter planar model is proposed for the optimization problem with multidimensional parameters and highly nonlinear constraints. Based on this visualization optimization method, a set of structural parameters is obtained, and the corresponding optimized workspace is illustrated too. Finally, the directions for future work are discussed in Section 5.

2. Structure of Humanoid Robotic Arm

2.1 Structural configuration of HRA

The mechanism diagram of the HRA is shown in Fig. 1(b), and the definition of structural parameters of the HRA is presented in Table I.

According to the spherical 5R parallel mechanism, the HSJ is composed of a fixed platform, an active platform, and two asymmetric kinematic chains (RRR and RR). The base reference frame O-XYZ and moving reference frame of the HSJ O-$X_1Y_1Z_1$ are both attached at the center O, which is the common intersection of the rotation axes. In the initial pose, the X, X_1 and OC_2 axes, the Y, Y_1 and OA_2 axes, and the Z, Z_1 and OC_1 axes are coincident, respectively.

The HEJ is a series 3-DOF kinematic chain RRR. The moving reference frame O_2-$X_2Y_2Z_2$ is attached at the center O_2, which is the common intersection of the rotation axes. In the initial pose, the X_1 and X_2 axes, the Y_1 and Y_2 axes, and the Z_1, Z_2 and OO_2 axes are coincident, respectively.

Based on the spherical 3-RRP parallel mechanism, the fixed and active platforms of the HWJ are restrained by three symmetrical kinematic chains RRP. The base reference frame of the HWJ O_3-$X_3Y_3Z_3$ and moving reference frame O_4-$X_4Y_4Z_4$ are both attached at the common center O_3 (O_4), which are the common intersection of the rotation axes and the normals of the prismatic pairs. In the initial pose, all the moving pair axes of each kinematic chain are in the same plane, respectively. The X_3 and X_4 axes are coincident and perpendicular to the plane $H_3O_3K_3$; the Y_3 and Y_4 axes are coincident in the plane $H_3O_3K_3$; the Z_3, Z_4 and O_2F axes are coincident.

2.2 Mobility analysis

As such, in the base coordinate system, the initial unit axis vectors of all the motion pairs of each humanoid joint can be obtained as

Table I *Structural parameters of HRA.*

Attribution	notation	Physical meaning	Initial value	Value range	Final value
HSJ	φ_1 (°)	The angle between the A_1OZ and A_2OZ planes, $\varphi_1 = 90°$	–	–	90
	φ_2 (°)	The angle between the Z and OA_1 axes	90	60-135	110
	φ_3 (°)	The angle between the OA_1 and OB_1 axes	90	60-120	90
	φ_4 (°)	The angle between the OB_1 axis and the A_1OZ plane, and decided by the formula $\cos\varphi_3 = \cos\varphi_4\cos(|\pi/2\text{-}\varphi_2|)$	–	–	90
	r_1 (mm)	The distance between the revolute pair C_1 (C_2) and the center point O. C_1 and C_2 are equidistant from O.	55	35-85	55
	r_2 (mm)	The distance between the revolute pair B_1 and the center point O	90	60-110	80
	r_3 (mm)	The distance between the revolute pair A_1 (A_2) and the center point O. A_1 and A_2 are equidistant from O.	90	80-130	100
HEJ	r_4 (mm)	The distance between the point O_2 and O	200	190-240	220
	r_5 (mm)	The distance between the points O_2 and O_3, and decided by the formula $r_5 = r_4 (r_4 + r_5)$	–	–	264
	$r_4 : r_5$	The process parameter	0.9	0.6-1.2	5/6
HWJ	φ_5 (°)	The intersection angle of the three symmetrical kinematic chains, $\varphi_5 = 120°$	–	–	120
	φ_6 (°)	The angle between the O_3H_j and Z_3 axes, $j = 1, 2, 3$	90	70-90	90
	φ_7 (°)	The angle between the O_3K_j and O_3H_j axes, $j = 1, 2, 3$	20	10-40	35
	φ_8 (°)	The moving range of the slider P_j, $j = 1, 2, 3$	90	60-120	120

$$
\begin{cases}
\boldsymbol{S}_{A_1} = (-\sin\varphi_2 \quad 0 \quad \cos\varphi_2)^{\mathrm{T}} \\
\boldsymbol{S}_{B_1} = (-\cos\varphi_4 \quad -\sin\varphi_4 \quad 0)^{\mathrm{T}} \\
\boldsymbol{S}_{C_1} = (0 \quad 0 \quad 1)^{\mathrm{T}}
\end{cases}
\begin{cases}
\boldsymbol{S}_{A_2} = (0 \quad 1 \quad 0)^{\mathrm{T}} \\
\boldsymbol{S}_{C_2} = (1 \quad 0 \quad 0)^{\mathrm{T}}
\end{cases}
$$

$$
\begin{cases}
\boldsymbol{S}_D = (0 \quad 0 \quad 1)^{\mathrm{T}} \\
\boldsymbol{S}_E = (1 \quad 0 \quad 0)^{\mathrm{T}} \\
\boldsymbol{S}_F = (0 \quad 0 \quad 1)^{\mathrm{T}}
\end{cases}
\begin{cases}
\boldsymbol{S}_{H_1} = (\sin\varphi_5 \sin\varphi_6 \quad \cos\varphi_5 \sin\varphi_6 \quad \cos\varphi_6)^{\mathrm{T}} \\
\boldsymbol{S}_{K_1} = (\sin\varphi_5 \sin(\varphi_6 - \varphi_7) \quad \cos\varphi_5 \sin(\varphi_6 - \varphi_7) \quad \cos(\varphi_6 - \varphi_7))^{\mathrm{T}} \\
\boldsymbol{S}_{P_1} = (-\sin(\pi/6) \quad -\cos(\pi/6) \quad 0)^{\mathrm{T}}
\end{cases}
$$

$$
\begin{cases}
\boldsymbol{S}_{H_2} = (-\sin\varphi_5 \sin\varphi_6 \quad \cos\varphi_5 \sin\varphi_6 \quad \cos\varphi_6)^{\mathrm{T}} \\
\boldsymbol{S}_{K_2} = (-\sin\varphi_5 \sin(\varphi_6 - \varphi_7) \quad \cos\varphi_5 \sin(\varphi_6 - \varphi_7) \quad \cos(\varphi_6 - \varphi_7))^{\mathrm{T}} \\
\boldsymbol{S}_{P_2} = (\sin(\pi/6) \quad -\cos(\pi/6) \quad 0)^{\mathrm{T}}
\end{cases}
\begin{cases}
\boldsymbol{S}_{H_3} = (0 \quad \sin\varphi_6 \quad \cos\varphi_6)^{\mathrm{T}} \\
\boldsymbol{S}_{K_3} = (1 \quad \sin(\varphi_6 - \varphi_7) \quad \cos(\varphi_6 - \varphi_7))^{\mathrm{T}} \\
\boldsymbol{S}_{P_3} = (1 \quad 0 \quad 0)^{\mathrm{T}}
\end{cases}
$$

$$(1)$$

According to the number and nature of DOF of each parallel mechanism, which was already analyzed in our previous work [11, 12], the HRA can be equivalent to a serial robotic arm, and its mechanism
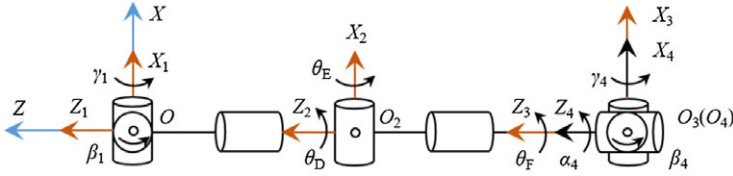
Figure 2. *Mechanism diagram of equivalent series robotic arm.*

diagram is shown in Fig. 2. β_1 and γ_1 denote the rotation input of the equivalent series shoulder joint around the Y_1 and X_1 axes, respectively. α_4, β_4, and γ_4 denote the rotation input of the equivalent series wrist joint around the Z_4, Y_4, and X_4 axes, respectively.

In addition, based on screw theory and exponential product formula, the homogeneous transformation matrix $\boldsymbol{g}_{04}$ for the forward displacement of the equivalent series robotic arm could be established as

$$
\begin{aligned}
\boldsymbol{g}_{04} = {} & \exp\left(\hat{\boldsymbol{\xi}}_{Y_1}, \beta_1\right) \cdot \exp\left(\hat{\boldsymbol{\xi}}_{X_1}, \gamma_1\right) \cdot \exp\left(\hat{\boldsymbol{\xi}}_{Z_2}, \theta_D\right) \cdot \\
& \exp\left(\hat{\boldsymbol{\xi}}_{X_2}, \theta_E\right) \cdot \exp\left(\hat{\boldsymbol{\xi}}_{Z_3}, \theta_F\right) \cdot \exp\left(\hat{\boldsymbol{\xi}}_{Z_4}, \alpha_4\right) \cdot \\
& \exp\left(\hat{\boldsymbol{\xi}}_{Y_4}, \beta_4\right) \cdot \exp\left(\hat{\boldsymbol{\xi}}_{X_4}, \gamma_4\right) \cdot \boldsymbol{g}_{04}\,(0)
\end{aligned}
\tag{2}
$$

where $\boldsymbol{g}_{04}(0)$ denotes the initial position orientation of the end platform in the base reference frame *O-XYZ*.

Furthermore, taken into account the inverse displacement analysis, Eq. (2) could be derived as

$$
\exp\left(\hat{\boldsymbol{\xi}}_{Y_1}, \beta_1\right) \cdot \exp\left(\hat{\boldsymbol{\xi}}_{X_1}, \gamma_1\right) \cdot \exp\left(\hat{\boldsymbol{\xi}}_{Z_2}, \theta_D\right) \cdot \exp\left(\hat{\boldsymbol{\xi}}_{X_2}, \theta_E\right) \cdot \boldsymbol{p}_{O_4} = \boldsymbol{p}_{st}
\tag{3}
$$

where $\boldsymbol{p}_{O_4}$ denotes the initial homogeneous position vector of point O_4, $\boldsymbol{p}_{st}$ denotes the homogeneous position vector of the space target point, and $\boldsymbol{p}_{st} = \boldsymbol{g}_{04} \cdot \boldsymbol{g}_{04}^{-1}(0) \cdot \boldsymbol{p}_{O_4}$.

According to Eqs. (2) and (3), the HSJ and HEJ (except for the revolute pair *F*) determine the position space of the end reference point O_4 and also provide a parasitic orientation for the end-moving platform. The revolute joint *F* of the HEJ and the HWJ determine the active orientation space of the end-moving platform.

3. Workspace Analysis

In this study, the position space of the end-reference point is decided by the orientation space of the HSJ and the position space of the HEJ, and the two parts do not affect each other without considering the external interference. Therefore, in order to make the workspace analysis specific and simple, the orientation space of the HSJ, the position space of the HEJ, and the active posture space of the end-moving platform are analyzed based on the coordinate search method to realize the workspace analysis of the proposed HRA.

3.1 Orientation space of HSJ

The displacement analysis of the HSJ and the position vectors of all the motion pairs are obtained as

$$
\begin{cases}
\beta_1 = \theta_{A_2} \\
\gamma_1 = \arctan(A/B)
\end{cases}
\tag{4}
$$
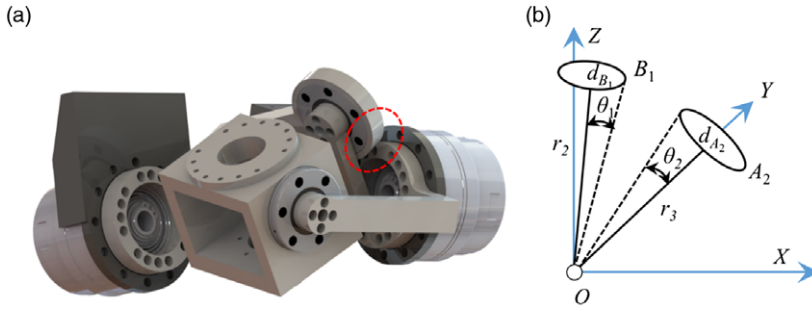
Figure 3. *Interference of rotation pairs B_1 and A_2: (a) Three-dimensional model; (b) interference principle.*

$$\begin{cases} A_1 = r_3 S_{A_1} \\ S_1 = r_2 \exp\left(\hat{S}_{A_1}, \theta_{A_1}\right) S_{B_1} \\ C_1 = r_1 S_{C_1} \\ A_2 = r_3 S_{A_2} \\ C_2 = r_1 \exp\left(\hat{S}_{Y_1}, \beta_1\right) \exp\left(\hat{S}_{X_1}, \beta_1\right) S_{C_2} \end{cases} \quad (5)$$

where $A = c\theta_{A_1}s\theta_{A_2}s\varphi_2 s\varphi_3 - s\theta_{A_2}s\varphi_2 c\varphi_3 + c\theta_{A_2}c\varphi_2 c\varphi_3 + c\theta_{A_1}s\theta_{A_2}c\varphi_2 s\varphi_3$, $B = s\theta_{A_1}s\varphi_3$, s, and c are the abbreviation of trigonometric function sin and cos, respectively.

There exist three main sets of basic mechanical constraints that limit the orientation space of the HSJ, viz.: (1) the interference of rotation pairs B_1 and A_2; (2) the link interference of $B_1 C_1$ and $A_2 C_2$; and (3) additional constraints related to the trunk movement characteristics. Let us make the assumption that the elements of the links and rotation pairs can be approximated by cylinders of radius d.

(1) The interference of rotation pairs B_1 and A_2: As shown in Fig. 3, the structure imposes a constraint, whose classification conditions as

$$f_1(\varphi_2, \varphi_3, r_2, r_3, \beta_1, \gamma_1) = \begin{cases} S_{B_1} \cdot S_{A_2} < \cos(\theta_1 + \theta_2) \\ S_{B_1} \cdot S_{A_2} > \cos(\theta_1 + \theta_2) \quad (r_2^2 + d_{B_1}^2) \le (r_3^2 + d_{A_2}^2) \end{cases} \quad (6)$$

where $\theta_1 = \arccos(r_2/\sqrt{r_2^2 + d_{B_1}^2})$, $\theta_2 = \arccos(r_3/\sqrt{r_3^2 + d_{A_2}^2})$.

(2) The link interference of $B_1 C_1$ and $A_2 C_2$: According to the structural characteristics of the HSJ, the constraint condition is established based on the complicated interference constraint of the moving link which detailed discussed by scholars [27]. As shown in Fig. 4, if the links $B_1 C_1$ and $A_2 C_2$ interfere, the intersection of the common perpendicular and the links must be on themselves, not on the extension line. Such that the critical conditions as

$$f_2(\varphi_2, \varphi_3, r_1, r_2, r_3, \beta_1, \gamma_1) = \{distance(B_1 C_1, A_2 C_2) \ge 2d_{link}\} \quad (7)$$

(3) Additional constraints related to the trunk movement characteristics: The robotic arm cannot collide with the torso during its movement, which is mainly determined by the posture space of the HSJ. The specific design imposes to consider the following constraint

$$f_3(\varphi_2, \varphi_3, \beta_1, \gamma_1) = \{distance(\text{upper arm}, \text{torso}) \ge d_{arm}\} \quad (8)$$

In addition, the search space is $\beta_1 \in [-\pi, \pi]$, $\gamma_1 \in [-\pi, \pi]$. The number of the point-group that contents the constraint conditions is taken as the workspace value (WSV) [27]. The simulation results developed in MATLAB code for the orientation space of the HSJ based on the initial structural parameters (as shown in Table I) are shown in Fig. 5. The forward flexion of the HSJ reaches 100° and the
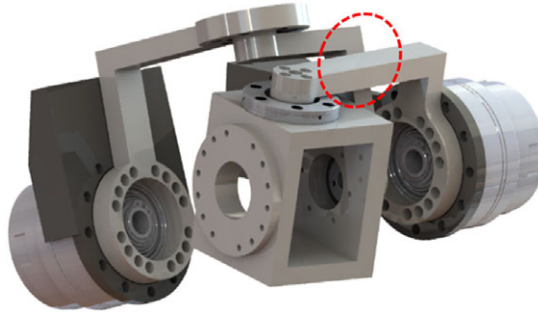
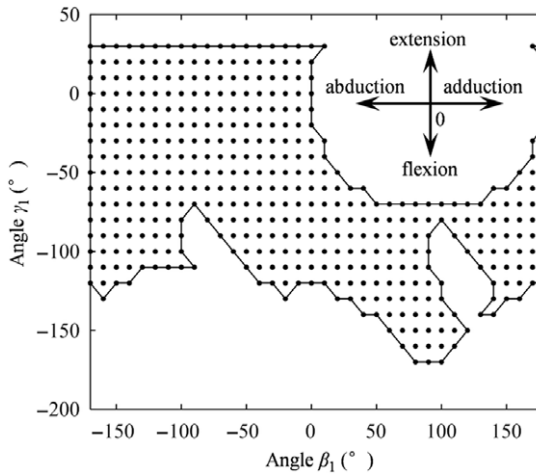**Figure 4.** *Link interference of B_1C_1 and A_2C_2.*

Figure 5. *Initial orientation space of HSJ.*

rear extension of the HSJ reaches 30° with the shoulder joint abduction. The adduction of the HSJ occurs simultaneously with the forward flexion of the HSJ. The coupling movements of the HSJ are in accordance with the kinematic characteristics of the human shoulder joint.

3.2 Position space of HEJ

The constraint condition is the rotation range of the revolute pair E, such that

$$f_4(\theta_E) = \{\|\theta_E\| \le 3\pi/4 \tag{9}$$

Thus, the search space is $\theta_D \in [-\pi, \pi]$, $\theta_E \in [-3/4\pi, 3/4\pi]$, and the volume of the point-group that satisfies the constraint conditions is taken as the WSV. The initial position space developed in MATLAB code is shown in Fig. 6. When a certain posture of the HSJ is given (as shown in Fig. 5, the HSJ located in the initial orientation), the volume of the position space is directly determined by r_5. Furthermore, the proportional relationship between r_4 and r_5 determines the extreme position of the end-reference point. Therefore, the appropriate ratio of r_4 and r_5 can be considered as one of the main factors affecting the volume of workspace.

3.3 Active orientation space

In order to describe the active orientation space more visually, the tilt-and-torsion angles proposed by Gosselin et al. [27] are adopted in this study. In this orientation representation, the moving platform is
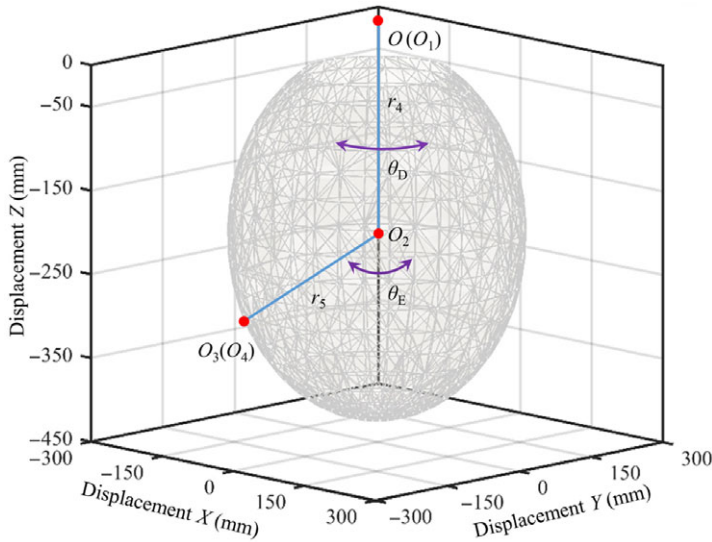
Figure 6. *Initial position space of HEJ.*

first rotated about the Z axis by an angle ϕ, then about the new Y axis by an angle θ, and finally about the new Z axis by an angle $\psi - \phi$. The search space is $\phi \in [-\pi, \pi]$, $\theta \in [0, \pi/2]$, $\psi \in [-\pi, \pi]$. The displacement analysis of the active orientation space is obtained as

$$\exp\left(\hat{\boldsymbol{\xi}}_F, \theta_F\right) \exp\left(\hat{\boldsymbol{\xi}}_{H_j}, \theta_{H_j}\right) \cdot \exp\left(\hat{\boldsymbol{\xi}}_{K_j}, \theta_{K_j}\right) \cdot \exp\left(\hat{\boldsymbol{\xi}}_{P_j}, \theta_{P_j}\right) = \exp\left(\hat{\boldsymbol{\xi}}_{Z_4}, \phi\right) \cdot \exp\left(\hat{\boldsymbol{\xi}}_{Y_4}, \theta\right) \cdot \exp\left(\hat{\boldsymbol{\xi}}_{Z'_4}, \psi\right)$$

(10)

where $j = 1, 2, 3$.

The constraint condition is the moving range of the prismatic pairs, such that

$$f_4(\varphi_6, \varphi_7, \varphi_8, \phi, \theta, \psi) = \begin{cases} (\varphi_6 - \varphi_7 - \varphi_8 - 5°) \leq \theta_{P_1} \leq (\varphi_6 - \varphi_7 - 5°) \\ -(\varphi_6 - \varphi_7 - 5°) \leq \theta_{P_2} \leq \varphi_8 - (\varphi_6 - \varphi_7 - 5°) \\ (\varphi_6 - \varphi_7 - \varphi_8 - 5°) \leq \theta_{P_3} \leq (\varphi_6 - \varphi_7 - 5°) \end{cases}$$

(11)

The volume of the point-group that fulfills the constraint conditions is taken as the WSV. The initial active orientation space developed in MATLAB code is shown in Fig. 7. As shown in Fig. 7 (a), the orientation space has a spiraling trend and changes periodically with ψ, with a period of 120°. According to Fig. 7 (b), $[0, \pi/4]$ is the dexterous range of θ. In addition, $\phi \in [\pi/4, \pi]$ and $[-3\pi/4, -\pi/4]$, the limit angle of θ is slightly reduced. As a whole, based on the initial structural parameters of the HWJ, the dexterous range of the active orientation space is $\phi \in [-\pi, \pi]$, $\theta \in [0, \pi/4]$, $\psi \in [-\pi, \pi]$.
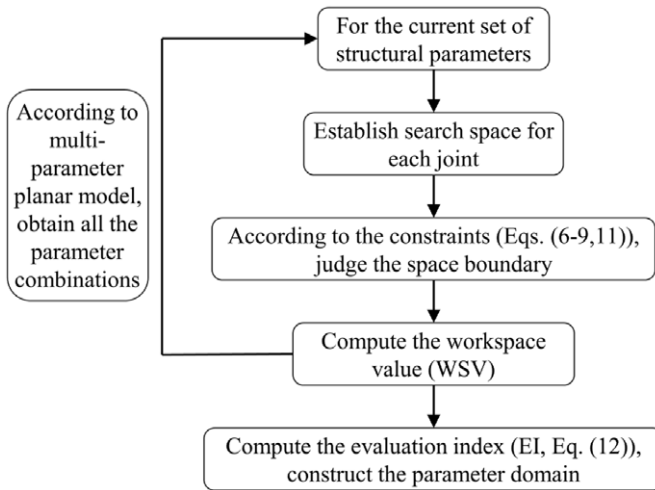
4. Workspace-Based Optimization

In order to realize the visualization design optimization of multiple parameters, a multi-parameter planar model is proposed, which could obtain all the parameter combinations. For a current set of structural parameters, the associated workspace and WSV are analyzed based on the aforementioned numerical method. Afterward, the evaluation index (EI) based on each group of structural parameters is calculated by computing the ratio of the corresponding WSV and RV, which represents the initial WSV also obtained in the previous section. Furthermore, based on the multi-parameter planar model, a set of structural parameters are obtained to realize the goal of increasing workspace, and its associated
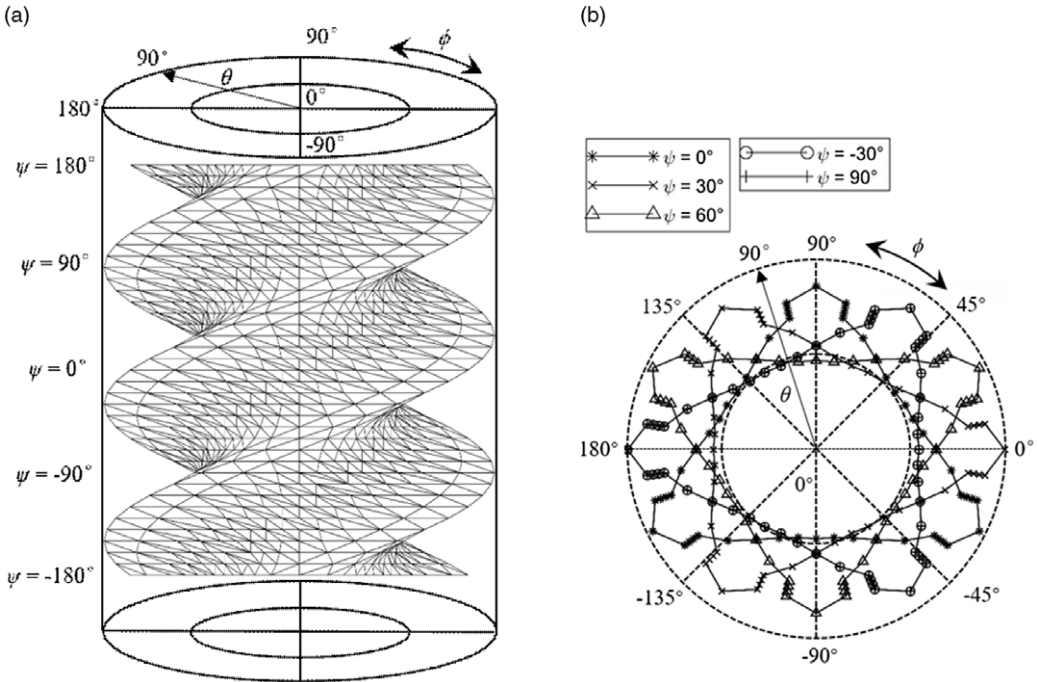
Figure 7. *Initial active orientation space of end-moving platform: (a) Perspective view; (b) top view with* $\psi = -30°, 0°, 30°, 60°,$ *and* $90°$.

Figure 8. *Flowchart describing optimization procedure.*

workspace is illustrated. This procedure is described schematically in Fig. 8, and the calculated formula about EI is

$$EI = \frac{WSV}{RV} \tag{12}$$

4.1 Multi-parameter planar mode

To further demonstrate the multi-parameter planar model, additional specifications are performed. It is assumed that there are L parameters, K sample points are taken for each parameter, and any two
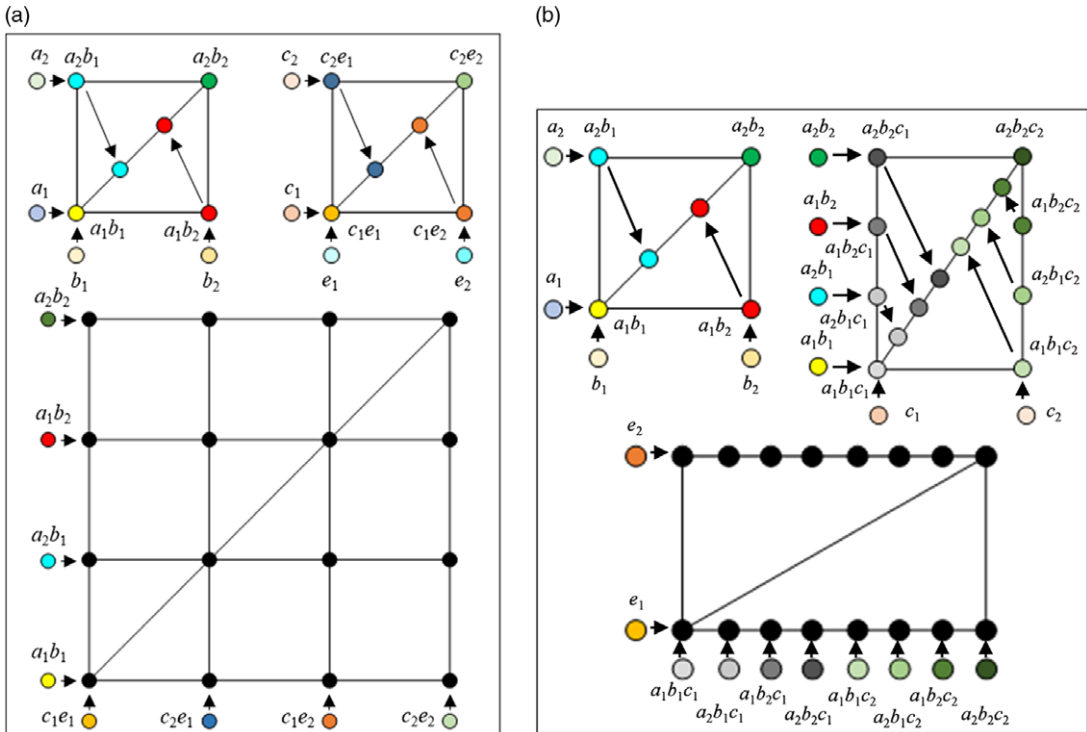
Figure 9. *Multi-parameter plane model: (a) model 1; (b) model 2.*

parameters are taken to form a square scatter diagram. Each intersection point of the square represents a combination, and these intersection points are mapped to a diagonal line. Any two diagonal lines are also formed into a new square (or rectangle) scatter diagram in accordance with the aforementioned method to obtain a new diagonal. This step is repeated until the last square (or rectangle) scatter diagram is obtained, whose intersection points contain the combination of all parameters. Note that the rectangular scatter diagram is caused by the fact that L is odd. Here, four parameters, a, b, c, and e, each of which takes the same number of sample points a_l, b_l, c_l, and e_l ($l = 1$, 2), are illustrated as an example, as shown in Fig. 9(a). It is worth noting that there is a similar method here. The main difference lies in a diagonal line and a new parameter to form a new rectangular scatter diagram, whose process is shown in Fig. 9(b).

4.2 Design optimization of HSJ

In the simulation analysis of this study, the value range for the structural parameters of the HSJ is presented in Table I, and parameters φ_2, φ_3, r_1, r_2, and r_3 are taken 7, 5, 6, 6, and 6 sample points, respectively, producing 7560 combinations as shown in Fig. 10(a). According to the visualization optimization algorithm developed in MATLAB code, the EIs based on each group of structural parameters are obtained, as shown in Fig. 10.

As shown in Fig. 10(b) and (c), the EI increases with the increases of r_3. The influence of r_2 on the EI is related to r_3, and the greater the difference between r_3 and r_2 is, the greater the EI is. As shown in Fig. 10(b) and (d), when $\varphi_3 \in [80°, 100°]$, φ_2 represents a negligible influence on the EI. When $\varphi_3 \in [60°, 80°]$ and $[100°, 120°]$, the EI decreases first and then increases as φ_2 increases. On the other hand, it is neither necessary nor possible to select the combination of parameters that maximizes EI. If the EI is greater than 1.45 (the maximum is 1.53), it is considered to achieve the goal of workspace-based optimization. Thus, considering the processing and assembling technology of the HSJ, a set of
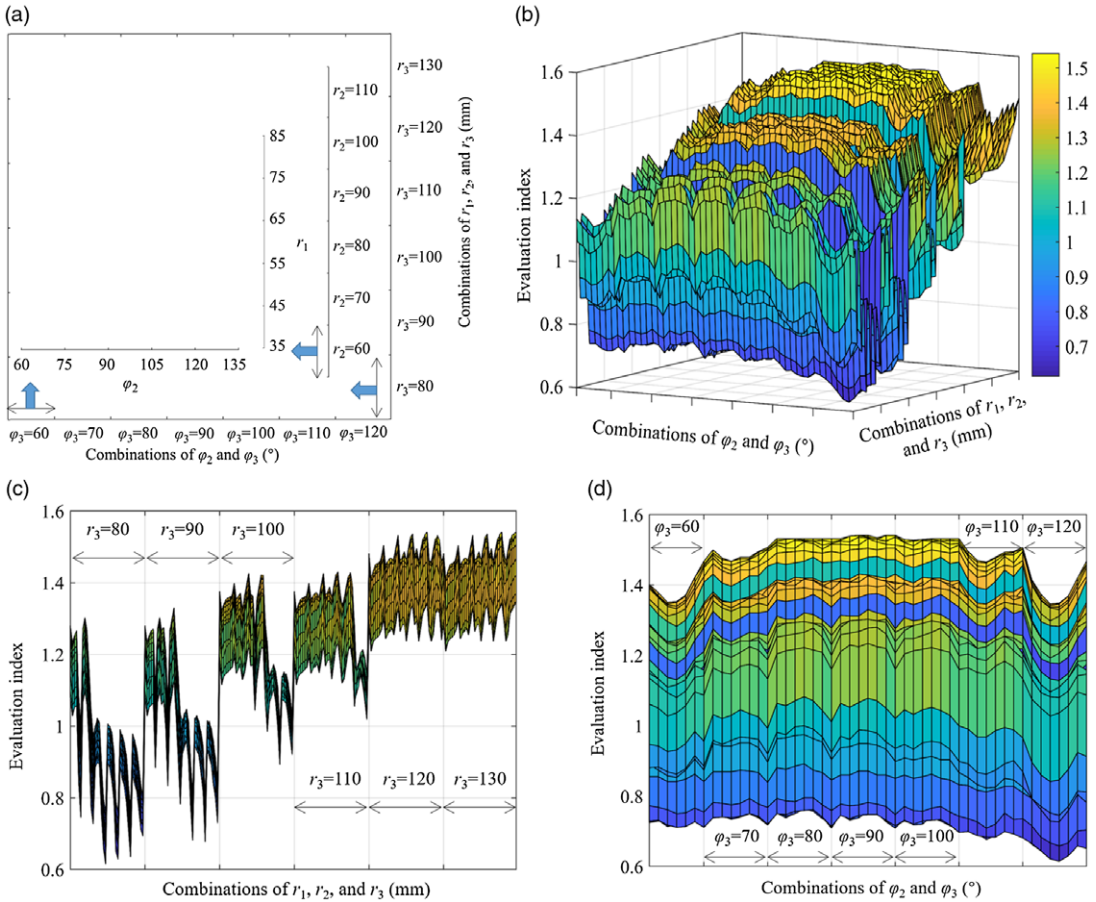
Figure 10. *Visualization design optimization of HSJ: (a) Parameter combinations; (b) perspective view; (c) left view; (d) front view.*

structural parameters is selected as $\varphi_2 = 110°$, $\varphi_3 = 90°$, $r_1 = 55$ mm, $r_2 = 80$ mm, and $r_3 = 100$ mm. The corresponding workspace is graphically represented in Fig. 11, which has significantly increased by a factor of 1.4. Compared with the initial posture space of the HSJ, the rear extension of the HSJ reaches 40° with the shoulder joint abduction. The adduction of HSJ occurs simultaneously with not only the forward flexion but also the rear extension of the HSJ.

4.3 Design optimization of HEJ

In the simulation analysis of this study, the value range for the structural parameters of the HWJ is presented in Table I, and parameters r_4 and $r_4 : r_5$ are taken 11 and 21 sample points, respectively, producing 231 combinations. According to the visualization optimization algorithm developed in MATLAB code, the EIs based on each group of structural parameters are obtained, as shown in Fig. 12.

As shown in Fig. 12(a) and (b), the EI increases rapidly as the ratio of r_4 and r_5 decreases. Especially when the ratio is less than 1, the growth rate increases swiftly. As shown in Fig. 12(a) and (c), when the ratio is greater than 0.9, the EI increases steadily with the increases of r_4. When the ratio is less than 0.9, the EI increases rapidly with the increases of r_4. As a whole, the smaller the ratio and the larger r_4, the larger the EI. If the EI is greater than 1.2, it is considered to achieve the goal of workspace-based optimization.
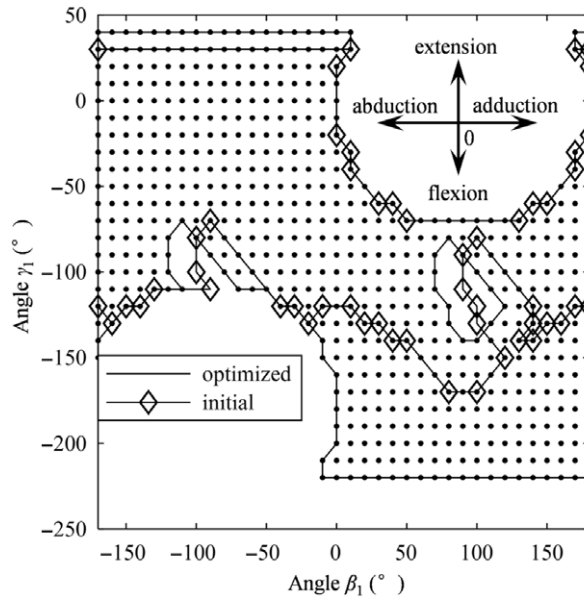
Figure 11. *Optimized orientation space of HSJ.*

On the other hand, in his work named Vitruvian Man, Leonardo da Vinci [28] developed 15 rules of proportion, which were used to model a human. Among these rules, the forearm, upper arm, and hand are 1/4, 1/8, and 1/10 of the height of a man, respectively. According to the aforementioned three rules, $r_4 : r_5 = 5 : 6$.

Therefore, the structural parameters of the HWJ must not only achieve the goal of workspace-based optimization but also conform to the structural characteristics of the human arm. Thus, based on a man with height of 1760 mm, $r_4 = 220$ mm and $r_5 = 264$ mm are obtained. The corresponding workspace is graphically represented in Fig. 13, which has significantly increased by the factor of 1.68.

4.4 Design optimization of HWJ

In the simulation analysis of this study, the value range for the structural parameters of HWJ is presented in Table I, and parameters φ_6, φ_7, and φ_8 are taken 11, 13, and 7 sample points, respectively, producing 1001 combinations. According to the visualization optimization algorithm developed in MATLAB code, the EIs based on each group of structural parameters are obtained, as shown in Fig. 14.

As shown in Fig. 14(a) and (b), the EI increases slightly with the increases in φ_8, and the effect of φ_7 on the EI is mainly related to φ_8. As shown in Fig. 14 (a) and (c), the EI increases with the increases in φ_6. When $\varphi_6 \in [70°, 75°]$, $\varphi_7 \in [30°, 40°]$, and $\varphi_8 \in [110°, 120°]$, the greater the difference between φ_6 and φ_7 is, the greater the EI is. If the EI is greater than 1.2(the maximum is 1.32), it is considered to achieve the goal of workspace-based optimization. Considering the compactness of the HWJ, a set of structural parameters is selected: $\varphi_6 = 90°$, $\varphi_7 = 35°$, and $\varphi_8 = 120°$. The corresponding workspace is graphically represented in Fig. 15, which has significantly increased by the factor of 1.3. The orientation space also has a spiraling trend and changes periodically with ψ, with a period of 120°. The limit angle of θ is slightly reduced to 80°. The dexterous range of the active orientation space is $\varphi \in [-\pi, \pi]$, $\theta \in [0, \pi/3]$, $\psi \in [-\pi, \pi]$.

Thus, all the structural parameters are obtained as follows: $\varphi_1 = 90°$, $\varphi_2 = 110°$, $\varphi_3 = 90°$, $\varphi_4 = 90°$, $\varphi_5 = 120°$, $\varphi_6 = 90°$, $\varphi_7 = 35°$, $\varphi_8 = 120°$, $r_1 = 55$ mm, $r_2 = 80$ mm, $r_3 = 100$ mm, $r_4 = 220$ mm, and $r_5 = 264$ mm, as listed in Table I.
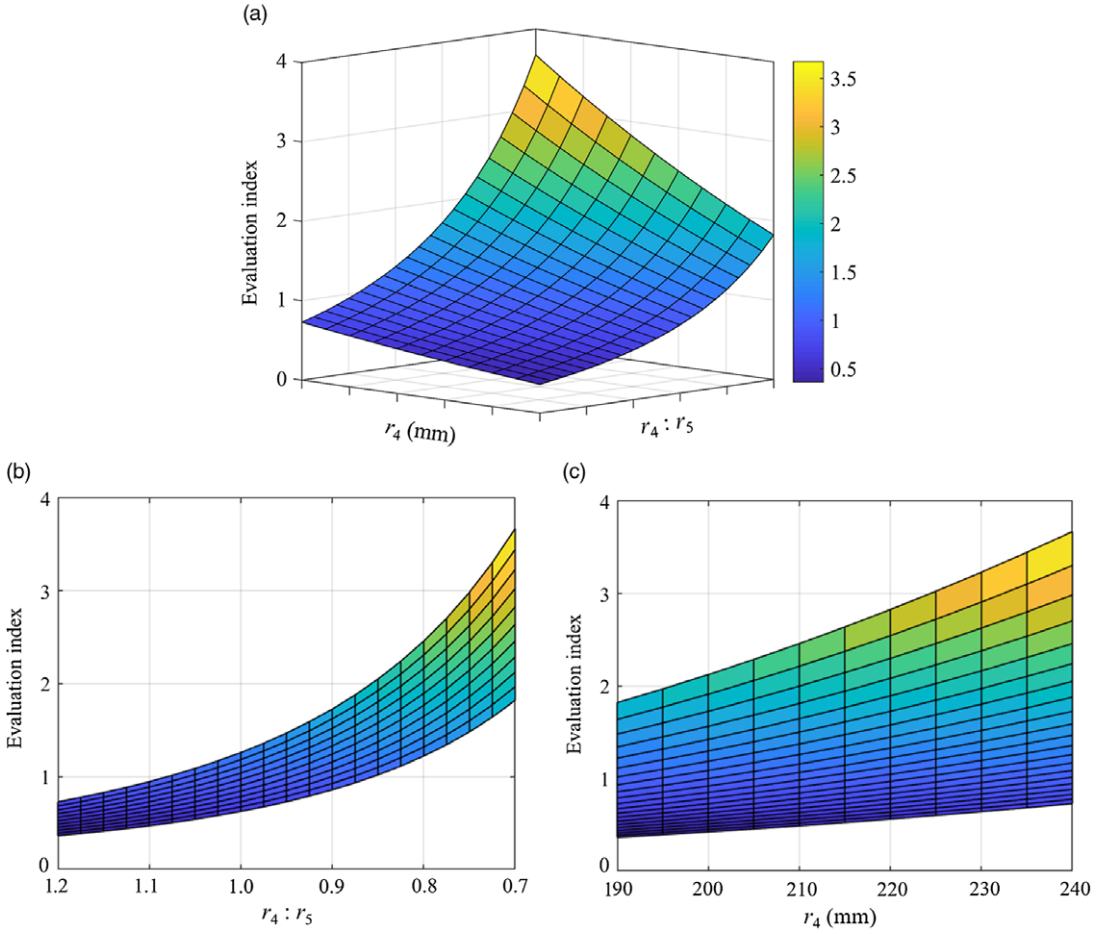
Figure 12. *Visualization design optimization of HWJ: (a) Perspective view; (b) left view; (c) front view.*
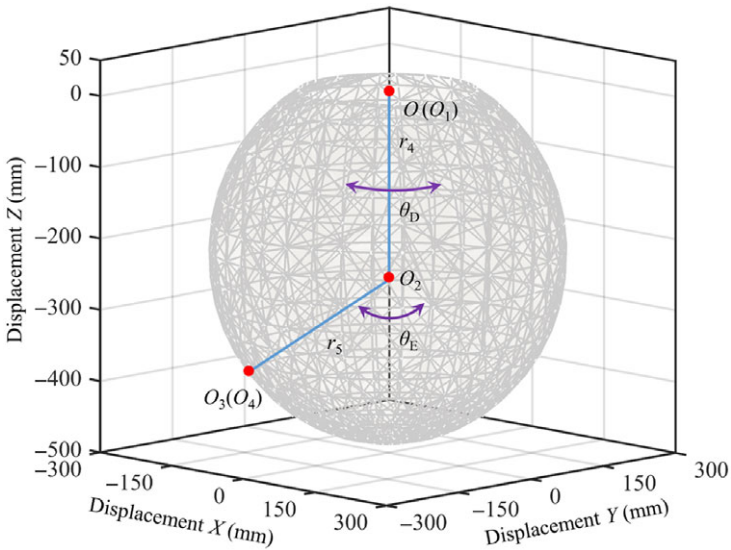

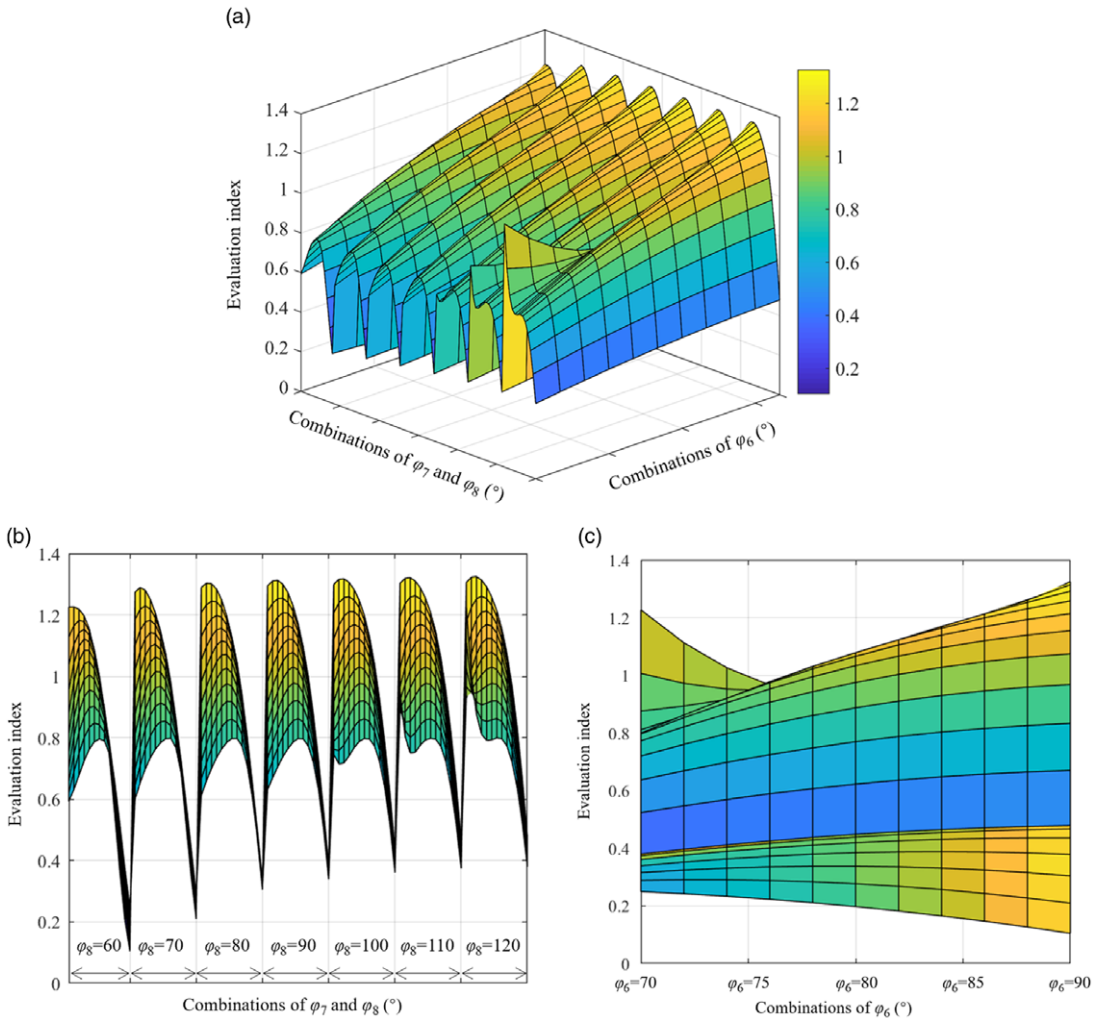**Figure 13.** *Optimized position space of the HEJ.*

Figure 14. *Visualization design optimization of HWJ: (a) Perspective; (b) left view; (c) front view.*

5. Conclusion

This study shows the workspace of each human joint of the hybrid robotic arm and studies the workspace-based parameter optimization based on the multi-parameter plane model. Considering the compactness and the processing and assembling technology of the mechanism, a set of structural parameters satisfying the workspace-based optimization objective is obtained.

The structural configuration of the hybrid robotic arm, which realizes the distribution of joints similar to that of a human arm, has the structural feature of workspace separation, providing researchers with more specific and clear information than the entire workspace analysis. In addition, the much larger active orientation space ensures the refined operation of the end manipulator. Furthermore, compared to other algorithms applied to parameter optimization, the multi-parameter planar model is proposed to the visualization design optimization of multiple parameters, which could demonstrate the coupling effect of parameters on the optimization target, instead of just getting a few numerical values of parameter combinations. Moreover, the obtained parameter domain can provide researchers with more combinations that meet other influencing factors.
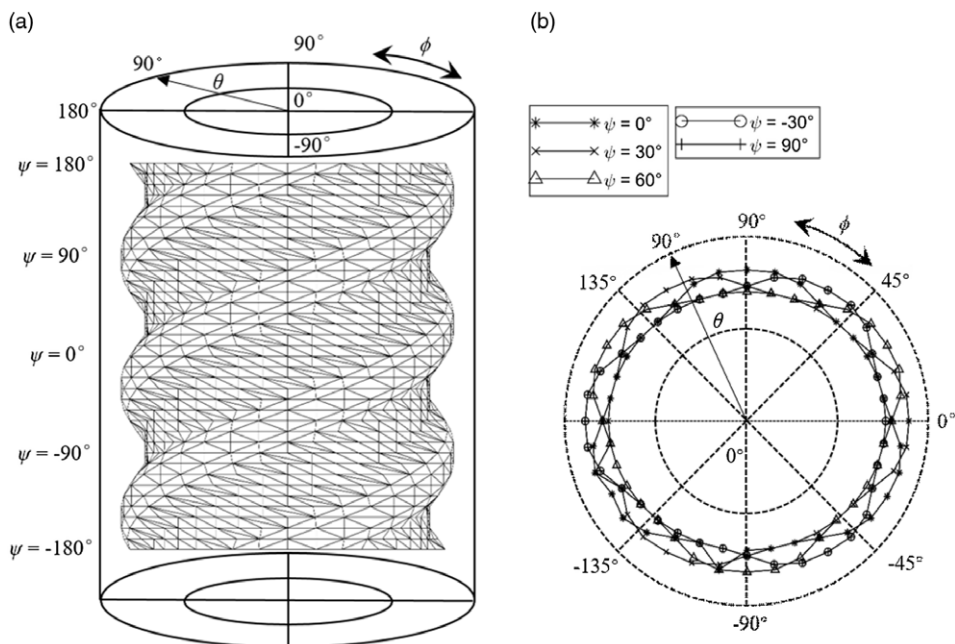
Figure 15. *Optimized active orientation space of end-moving platform: (a) Perspective view; (b) top view with* $\psi = -30°$, $0°$, $30°$, $60°$, *and* $90°$.

It is worth noting that the structural parameters selected based on the workspace optimization in this study do not necessarily lead to the optimal kinematic performance of the HRA. Therefore, the kinematics and dynamics of the hybrid mechanism and the corresponding performance index will be studied by the authors in the future. In addition, multi-objective optimization based on the multi-parameter planar model remains an open issue also worth further study.

Conflict of Interest. The authors declare none.

Ethical Considerations. The authors declare none.

Authors' Contributions. YL supervised the entire trial; PS wrote the manuscript; KS, YY, and BW assisted in sampling and laboratory analyses. All authors read and approved the final manuscript.

References

[1] M. A. Costa, B. Wullt, M. Norrlof and S. Gunnarsson, "Failure detection in robotic arms using statistical modeling, machine learning and hybrid gradient boosting," *Measurement* **146**, 425–436 (2019).

[2] X.-L. Chen and J.-Y. Guo, "Effects of spherical clearance joint on dynamics of redundant driving spatial parallel mechanism," *Robotica* **39**(6), 1064–1080 (2021).

[3] W. Ye and Q.-C. Li, "Type synthesis of lower mobility parallel mechanisms: A review," *Chin. J. Mech. Eng.* **32**(1), 38 (2019).

[4] J. Wei and J.-S. Dai, "Lie group based type synthesis using transformation configuration space for reconfigurable parallel mechanisms with bifurcation between spherical motion and planar motion," *J. Mech. Des.* **142**(6), 063302 (2020).

[5] Q.-Z. Meng, F.-G. Xie, X.-J. Liu and Y. Takeda, "Screw theory-based motion/force transmissibility analysis of high-speed parallel robots with articulated platforms," *ASME J. Mech. Robot.* **12**(4), 041011 (2020).

[6] H. Li, Q.-S. Xu, S.-M. Wen, X.-D. Qin and T. Huang, "Deformation analysis and hole diameter error compensation for hybrid robot based helical milling," *J. Adv. Mech. Des. Syst. Manuf.* **13**(2), 18–00461 (2019).

[7] R. Datouo, M. Ahanda, A. Melingui, F. Biya-Motto and B. E. Zobo, "Adaptive fuzzy finite-time command-filtered backstepping control of flexible-joint robots," *Robotica* **39**(6), 1081–1100 (2021).

[8] T. Sun, B.-B. Lian, Y.-M. Song and L. Feng, "Elastodynamic optimization of a 5-DoF parallel kinematic machine considering parameter uncertainty," *IEEE-ASME Trans. Mechatron.* **24**(1), 315–325 (2019).

[9] N. Baron, A. Philippides and N. Rojas, "On the false positives and false negatives of the Jacobian matrix in kinematically redundant parallel mechanisms," *IEEE Trans. Robot.* **36**(3), 951–958 (2020).

[10] T. Sun and S.-F. Yang, "An approach to formulate the Hessian matrix for dynamic control of parallel robots," *IEEE-ASME Trans. Mechatron.* **24**(1), 271–281 (2019).

[11] P. Sun, Y.-B. Li, Z.-S. Wang, K. Chen, B. Chen, X. Zeng, J. Zhao and Y. Yue, "Inverse displacement analysis of a novel hybrid humanoid robotic arm," *Mech. Mach. Theory* **147**, 103743 (2020).

[12] P. Sun, Y.-B. Li, K. Chen, W.-T. Zhu, Q. Zhong and B. Chen, "Generalized kinematics analysis of hybrid mechanisms based on screw theory and lie groups lie algebras," *Chin. J. Mech. Eng.* **34**, 98 (2021).

[13] H.-F. Ding, C.-W. Cai, Z.-M. Chen, T. Ke and B.-W. Mao, "Configuration synthesis and performance analysis of 9-speed automatic transmissions," *Chin. J. Mech. Eng.* **33**(1), 50 (2020).

[14] V. Garcia-Marina, I. F. de Bustos, G. Urkullu and R. Ansola, "Optimum dimensional synthesis of planar mechanisms with geometric constraints," *Meccanica* **55**(11), 2135–2158 (2020).

[15] C. Zhao, H.-W. Guo, R.-Q. Liu, Z.-Q. Deng, B. Li and J. Tian, "Actuation distribution and workspace analysis of a novel 3(3RRlS) metamorphic serial-parallel manipulator for grasping space non-cooperative targets," *Mech. Mach. Theory* **139**, 424–442 (2019).

[16] H. L. Vieira, J. V. C. Fontes, A. T. Beck and M. M. da Silva, "Reliable and failure-free workspaces for motion planning algorithms for parallel manipulators under geometrical uncertainties," *J. Comput. Nonlinear Dyn.* **14**(2), 021005 (2019).

[17] R. S. Novin, M. T. Masouleh and M. Yazdani, "A new neural gas network approach for obtaining the singularity-free workspace of 3-DOF planar parallel manipulators, Proc. Inst. Mech. Eng. Part C-J. Eng. Mech. Eng. Sci. **232**(1), 174–189 (2018).

[18] W. Li, J. Angeles and F. Gao, "The kinematics and design for quasi-isotropy of 3U serial manipulators with reduced wrists," *Mech. Mach. Theory* **154**, 104035 (2020).

[19] Q.-Z. Meng, F.-G. Xie, X.-J. Liu and Y. Takeda, "An evaluation approach for motion-force interaction performance of parallel manipulators with closed-Loop passive limbs," *Mech. Mach. Theory* **149**, 103844 (2020).

[20] E. K. Yasojima, R. C. de Oliveira, O. N. Teixeira and R. L. Pereira, "CAM-ADX: A new genetic algorithm with increased intensification and diversification for design optimization problems with real variables," *Robotica* **37**(9), 1595–1640 (2019).

[21] H.-P. Shen, D. Chablat, B.-X. Zeng, J. Li, G.-L. Wu and T.-L. Yang, "A translational three-degrees-of-freedom parallel mechanism with partial motion decoupling and analytic direct kinematics," *ASME J. Mech. Robot.* **12**(2), 021112 (2020).

[22] A. Chatterjee, "Differential evolution tuned fuzzy supervisor adapted extended Kalman filtering for SLAM problems in mobile robots," *Robotica* **27**(3), 411–423 (2009).

[23] Y.-J. Lou, Y.-S. Zhang, R.-N. Huang, X. Chen and Z.-X. Li, "Optimization algorithms for kinematically optimal design of parallel manipulators," *IEEE Trans. Autom. Sci. Eng.* **11**(2), 574–584 (2014).

[24] S. H. Lee, G. Eoh and B. H. Lee, "Relational FastSLAM: A parameter dimension reduction-based estimation approach to enhance the kinematic accuracy of a parallel hardware-in-the-loop docking simulator," *Robotica* **34**(6), 1282–1296 (2016).

[25] I. Khemili, M. A. Ben Abdallah and N. Aifaoui, "Multi-objective optimization of a flexible slider-crank mechanism synthesis, based on dynamic responses," *Eng. Optimiz.* **51**(6), 978–999 (2019).

[26] C. Yang, Q.-C. Li and Q.-H. Chen, "Multi-objective optimization of parallel manipulators using a game algorithm," *Appl. Math. Model.* **74**, 217–243 (2019).

[27] B. Monsarrat and C. M. Gosselin, "Workspace analysis and optimal design of a 3-leg 6-DOF parallel platform mechanism," *IEEE Trans. Robot. Autom.* **19**(6), 954–966 (2003).

[28] C. M. Oranges, R. D. Largo and D. J. Schaefer, "Leonardo da Vinci's Vitruvian Man: The ideal human proportions and man as a measure of all things," *Plast. Reconstr. Surg.* **137**(4), 764E–165E (2016).